Intercomparison of flux-, gradient-, and variance-based optical turbulence (Cn 2) parameterizations

Pierzyna, Maximilian; Hartogensis, Oscar; Basu, Sukanta ; Saathof, Rudolf

DOI
10.1364/AO.519942

Publication date
2024

Document Version
Final published version

Published in
Applied Optics

Citation (APA)
Pierzyna, M., Hartogensis, O., Basu, S., & Saathof, R. (2024). Intercomparison of flux-, gradient-, and variance-based optical turbulence (Cn 2) parameterizations. *Applied Optics*, *63*(16), E107-E119. https://doi.org/10.1364/AO.519942

applied optics

Intercomparison of flux-, gradient-, and variance-based optical turbulence (C_n^2) parameterizations

Maximilian Pierzyna,[1,*] **Oscar Hartogensis,**[2] **Sukanta Basu,**[3,4] **and Rudolf Saathof**[5]

[1]Department of Geoscience and Remote Sensing, Delft University of Technology, 2628 CN Delft, The Netherlands
[2]Department of Environmental Sciences, Wageningen University & Research, 6700 HB Wageningen, The Netherlands
[3]Atmospheric Sciences Research Center, University at Albany, Albany, New York 12222, USA
[4]Department of Environmental and Sustainable Engineering, University at Albany, Albany, New York 12222, USA
[5]Faculty of Aerospace Engineering, Delft University of Technology, 2629 HS Delft, The Netherlands
*m.pierzyna@tudelft.nl

Received 5 February 2024; revised 12 April 2024; accepted 24 April 2024; posted 24 April 2024; published 22 May 2024

For free-space optical communication or ground-based optical astronomy, ample data of optical turbulence strength (C_n^2) are imperative but typically scarce. Turbulence conditions are strongly site dependent, so their accurate quantification requires *in situ* measurements or numerical weather simulations. If C_n^2 is not measured directly (e.g., with a scintillometer), C_n^2 parameterizations must be utilized to estimate it from meteorological observations or model output. Even though various parameterizations exist in the literature, their relative performance is unknown. We fill this knowledge gap by performing a systematic three-way comparison of a flux-, gradient-, and variance-based parameterization. Each parameterization is applied to both observed and simulated meteorological variables, and the resulting C_n^2 estimates are compared against observed C_n^2 from two scintillometers. The variance-based parameterization yields the overall best performance, and unlike other approaches, its application is not limited to the lowest part of the atmospheric boundary layer (i.e. the surface layer). We also show that C_n^2 estimated from the output of the Weather Research and Forecasting model aligns well with observations, highlighting the value of mesoscale models for optical turbulence modeling.

https://doi.org/10.1364/AO.519942

1. INTRODUCTION

Free-space optical communication (FSOC) is a key technology for supporting the increasing needs of our densely connected, data-heavy world by providing energy-efficient, secure links with high-data transmission capacity at potentially low cost. In contrast to traditional radio frequency communication, FSOC transmits data with an optical beam that propagates through the atmosphere. This propagating beam is disturbed by various atmospheric phenomena, such as clouds, molecular and aerosol scattering, and fluctuations of the atmospheric refractive index, the so-called optical turbulence (OT) [1]. Data of these OT conditions are highly relevant for designing and deploying reliable, high-performance FSOC links, but their availability is typically scarce. Therefore, there is an urgent need to quantify the OT conditions well [2].

Since turbulence strongly depends on the local topography and the ever-changing meteorological conditions, site-specific estimations of the turbulence conditions are complex. As a result, the performance quantification of an FSOC link requires either measuring or modeling the OT strength (C_n^2) for the time of day and the site of (envisioned) operation. Such C_n^2 measurements are performed directly using scintillometers or indirectly through standard meteorological instruments in conjunction with a C_n^2 parameterization. While scintillometers directly measure the intensity fluctuations of light propagating through the turbulent atmosphere [3], the parameterizations of the indirect approach link C_n^2 to variables of the processes causing the OT—wind shear and buoyancy [4]. Similarly, these parameterizations also allow the estimation of C_n^2 from atmospheric mesoscale simulations in a post-processing step [5,6]. In practice, direct scintillometer measurements are often not available, so the parameterizations are commonly used on observed (see, e.g., [4,7–9]) and simulated meteorological data (see, e.g., [6,10–14]), and a multitude of such C_n^2 parameterizations exists (see [15,16] for an extensive overview). However, their accuracy compared to scintillometer observations is unclear a priori, and studies in literature often do not motivate their choice of one parameterization over another.

In the present work, we aim to address this issue by intercomparing the performance of C_n^2 parameterizations from three main classes. Multiple test cases representing different seasonal conditions are selected for which scintillometer-based C_n^2 time series are available. These observations serve as the best possible ground truth. The scintillometers are deployed at the Cabauw Experimental Site of Atmospheric Research (CESAR) site [17] in the Netherlands, where a recent FSOC test campaign [18] was conducted. That site is also equipped with reliable and well-maintained instruments from which we obtain standard meteorological measurements, collocated and concurrent with the scintillometer data. Additionally, we run a mesoscale simulation for each test case to reproduce the meteorology at the time and location of the scintillometer observations. These observed and simulated meteorological variables are inputs to the different C_n^2 parameterizations, and the resulting C_n^2 estimates are compared to the scintillometer measurements for performance assessment. Having two sources of meteorological data can help us to differentiate errors coming from the parameterizations themselves from errors due to limitations of instrumentation or simulation. It also enables us to systematically evaluate the feasibility of mesoscale simulations for C_n^2 estimation in an FSOC context.

2. METHODOLOGY

We need diverse and reliable underlying datasets to conduct a comprehensive intercomparison of C_n^2 parameterizations. As a baseline, we utilize C_n^2 observations from two scintillometers mounted at two different heights (cf. Section 2.B), which enable us to assess height dependencies in the performance of the C_n^2 parameterizations. Two high-quality meteorological datasets—concurrent and collocated with the scintillometer measurements—serve as parameterization inputs. One dataset is obtained experimentally at the CESAR site (cf. Section 2.C), while the other one is a mesoscale hindcast of the same time and location produced by the Weather Research and Forecasting (WRF) [19] model (cf. Section 2.D). Three C_n^2 parameterizations from different classes are applied to the input data for an intercomparison between estimated and observed C_n^2 as visualized in Fig. 1. The specific parameterizations representing these three classes—flux-, gradient-, and variance-based—are presented in Section 2.A.

Our methodology is applied to three test cases covering spring (April 18–22, 2022; 4 days), summer (July 27–29, 2022; 2 days), and autumn (October 8–10, 2022; 2 days). By spreading the test cases throughout the year, we aim to assess whether seasonal dependencies exist in the performance of the different C_n^2 parameterizations. All test cases are subject to calm synoptic conditions and a mostly clear sky at the CESAR site. Selecting such favorable meteorological conditions is essential because the present study aims to assess the performance of the C_n^2 parameterizations, not the performance of the deployed instruments or the mesoscale models for various impactful weather events. Precipitating events, for example, are challenging to simulate, and scintillometers cannot conduct measurements when visibility is low, for instance, during heavy rain or fog. Since the Dutch weather during winter is cloudy, rainy, and/or foggy, no suitable winter test case could be identified for the CESAR site.

A. C_n^2 Estimation from Observed and Simulated Meteorology

The strength of OT is quantified through C_n^2, the refractive index structure function parameter. C_n^2 describes the refractive index variations caused by density fluctuations due to temperature and humidity fluctuations. If the parameter is not measured directly with a scintillometer, it can, therefore, be derived from C_T^2, the temperature structure function parameter, utilizing the Gladstone relationship [20]:

$$C_n^2 = \left(A\frac{P}{T^2}\right)^2 \left(1 + \frac{0.03}{\beta}\right)^2 C_T^2. \tag{1}$$

Here, $A \approx 7.9 \times 10^{-5}$ K hPa^{-1} is almost constant for optical wavelengths [21], P is the station pressure in hPa, T is the air temperature in K, and $\beta = Q_H/Q_L$ is the Bowen ratio. By balancing the dynamic sensible heat flux Q_H with the latent heat flux Q_L, the Bowen ratio term accounts for the influence of moisture on C_n^2 [22]. During neutral atmospheric conditions (sunrise/sunset), Q_H and β change signs twice a day, leading to unrealistically dominant moisture correction factors. This mathematical singularity is avoided by truncating β to ± 0.1 for $|\beta| < 0.1$. We also note that the $(1 + 0.03/\beta)^2$ moisture correction can introduce an overcorrection by a factor of ~4 around these neutral conditions due to the assumed correlation of moisture flux and heat flux ($|R_{Tq}| = 1$) in the derivation of the correction. The interested reader is referred to [23] for a detailed discussion, but for FSOC applications, the correction

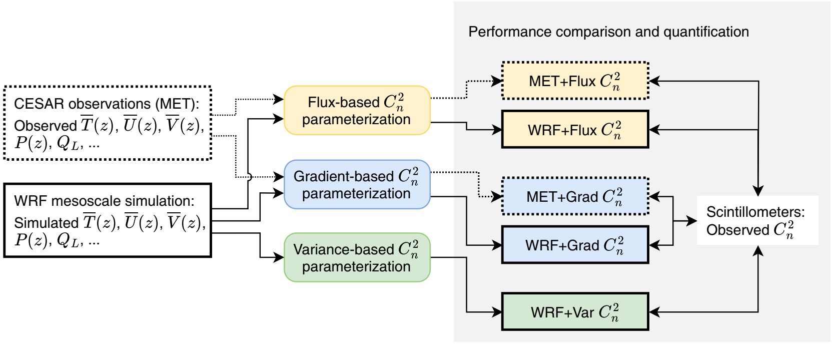

Fig. 1. Schematic of the three-way performance comparison and quantification applied in this study. For each test case, C_n^2 is estimated with different parameterizations (round boxes) from observed (MET) and simulated (WRF) meteorology and compared to scintillometer observations.

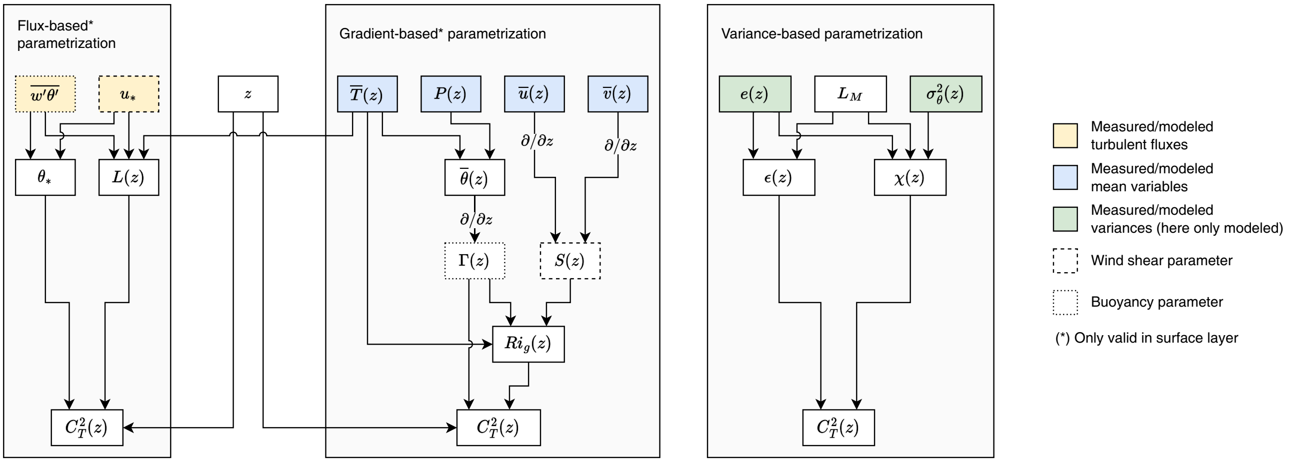

Fig. 2. Dependency of C_T^2 on measured or modeled input parameters for the three types of C_T^2 parameterizations.

presented in Eq. (1) is considered adequate. That is because neutral conditions do not prevail long and are subject to very weak turbulence, so correction errors have low practical relevance. In addition, a more accurate correction requires additional atmospheric water vapor measurements, which is impractical in an FSOC context.

Due to the discussed relation between C_n^2 and C_T^2, the methods presented in the following only parameterize C_T^2, which is defined as the coefficient of the second-order structure function of temperature T in the inertial range as

$$C_T^2 = \left\langle [T(x) - T(x+r)]^2 \right\rangle / r^{2/3}, \tag{2}$$

Where $\langle \square \rangle$ denotes the ensemble average. The structure-function approach requires a high-frequency temperature signal (>10 Hz) to capture the fast-evolving turbulence, which is often infeasible to obtain through measurements or simulations. Therefore, various parameterizations were developed to estimate C_T^2 from more routinely available data. These parameterizations can be broadly classified by the type of information they use—flux-, gradient-, or variance-based methods, as shown in Fig. 2.

All parameterizations aim at capturing the two processes modulating turbulence—wind shear and buoyancy [24]—but utilize different types of physical variables (cf. dashed and dotted boxes in Fig. 2). The difference between the variables is whether they represent the slowly varying mean or the fast-changing fluctuations of a turbulent flow field. For example, the space and time-dependent potential temperature field $\theta(t, x, y, z)$ can be decomposed into mean potential temperature $\bar{\theta}$ and turbulent fluctuations θ' so that $\theta(t, x, y, z) = \bar{\theta}(x, y, z) + \theta'(t, x, y, z)$ [24]. Similarly, the wind components u, v, and w can be decomposed into the mean field $(\bar{u}, \bar{v}, \bar{w})$ and fluctuations (u', v', w'). While gradient-based C_n^2 methods only use vertical gradients of the mean quantities, the flux and variance-based approaches require knowledge about turbulent fluxes (e.g., a momentum flux $\overline{u'w'}$) or turbulent variances (e.g., potential temperature variance $\overline{\theta'\theta'} = \sigma_\theta^2$) formed from the fluctuation components of the fields. These mean quantities, fluxes, and variances can be observed experimentally or simulated using mesoscale models, such as the WRF model.

1. Flux-based Method

One approach of linking buoyancy and wind shear to the temperature fluctuations (i.e., C_T^2) is by utilizing the sensible heat flux $\overline{w'\theta'}$ and the friction velocity u_*, respectively. The latter has the unit m s^{-1} and is called a velocity but is a function of two components of the turbulent vertical momentum flux: $u_* = (\overline{u'w'}^2 + \overline{v'w'}^2)^{1/4}$. Wyngaard *et al.* [4] proposed a flux-based parameterization (W71-flux) based on these quantities and Monin–Obukhov similarity theory (MOST) given as

$$C_T^2 = T_*^2 z^{-2/3} g(\zeta), \tag{3}$$

where $T_* = -\overline{w'\theta'}/u_*$ is the temperature scale. The similarity function g

$$g(\zeta) = 4.9(1 - 6.1\zeta)^{-\frac{2}{3}}, \quad \zeta < 0,$$

$$g(\zeta) = 4.9\left(1 + 2.2\zeta^{\frac{2}{3}}\right), \quad \zeta \geq 0, \tag{4}$$

depends on the stability parameter $\zeta = z/L$ with Obukhov length $L = -u_*^3 \bar{T}/(\kappa g \overline{w'\theta'})$ and height above ground z. In L, $g = 9.81$ m s^{-2} is the gravitational acceleration of Earth, $\kappa = 0.4$ is the Von Kármán constant, $\bar{T}$ is the mean air temperature in K, and $\overline{w'\theta'}$ is the kinematic sensible heat flux in m K s^{-1}. The coefficients of Eq. (4) are empirically determined and vary in literature [16]. We use the coefficients presented by Andreas [7], who adjusted the original W71-flux coefficients for $\kappa = 0.4$. Friction velocity and sensible heat flux are surface variables available from the WRF model and a sonic anemometer at the CESAR site [17].

2. Gradient-based Method

Measuring fluxes require sonic anemometers that record high-frequency temperature and velocity signals. If such instruments are unavailable, a set of vertically separated standard thermometers and anemometers can be used for C_T^2 estimation in conjunction with a gradient-based method. These slow-response instruments yield the temporal evolution of the mean temperature and mean wind profiles. The vertical gradients of (potential) temperature and horizontal wind represent the buoyancy and shear contributions to turbulence, respectively. Wyngaard *et al.* [4] also presented a gradient-based C_T^2 parameterization:

$$C_T^2 = z^{4/3}\Gamma^2 f\left(\mathrm{Ri}_g\right). \quad \textbf{(5)}$$

Here, f is a similarity function depending on the gradient Richardson number $\mathrm{Ri}_g = (g/\bar{\theta})(\Gamma/S^2)$, and the mean potential temperature gradient $\Gamma = \partial\bar{\theta}/\partial z$. The stability parameter Ri_g is a ratio balancing buoyancy, captured through Γ, and the mean wind shear $S = \sqrt{(\partial\bar{u}/\partial z)^2 + (\partial\bar{v}/\partial z)^2}$. Thus, Γ and S fulfill the same role of including buoyancy and shear modulation of the turbulence into the gradient-based formulation like u_* and $\overline{w'\theta'}$ do for W71-flux. The empirical similarity function $f(\mathrm{Ri}_g)$ in Eq. (5) is tabulated by Wyngaard *et al.*, but He and Basu [25] presented an improvement of f for stably stratified conditions ($\mathrm{Ri}_g > 0$) based on direct numerical simulations given as

$$f(\mathrm{Ri}_g) = 0.05 + 1.02\exp(-14.49\mathrm{Ri}_g), \quad \mathrm{Ri}_g > 0. \quad \textbf{(6)}$$

We use this improved formulation for stable conditions and a spline interpolation of the original W71 values only for unstable atmospheric conditions ($\mathrm{Ri}_g \leq 0$). This combined approach is abbreviated as W71/HB16-grad for this work.

All required mean variables (cf. Fig. 2) are routinely available both as time-varying 3D fields from the WRF model and as time series observed at multiple heights at the CESAR site. The gradients are typically strongest close to the ground [24], so we aim to accurately compute the lowest gradients numerically by adding the following information: For S, we assume a logarithmic wind profile close to the surface so that $u(z_0) = v(z_0) = 0$ with surface roughness length z_0 (known from WRF or experiments [26]). For Γ, we employ the 2 m potential temperature $\bar{\theta}_2$ provided by WRF's surface layer scheme or the 2 m thermometer deployed at CESAR. Section 1 of Supplement 1 explains these technicalities in more detail.

3. Surface Layer Assumption

Like the W71-flux parameterization, the gradient-based W71/HB16-grad approach is based on MOST. As a result, both approaches inherit the MOST limitation that they are only applicable within the atmospheric surface layer (SL), which is defined as 10% of the atmospheric planetary boundary layer (PBL) height [24]. MOST assumes that fluxes within the SL are invariant with height, which is not valid anymore for the upper part of the boundary layer. The height of the PBL and, consequently, the SL changes throughout the day. Typically, the SL is shallow during the night (∼10 m) and deep during the day (∼100 m) [24], so the height until which the gradient and the flux-based methods can be applied also changes.

4. Variance-based Method

A physics-based parameterization that is valid beyond the SL follows from dimensional analysis using Corrsin's [27] expression and Kolmogorov's [28] universal spectrum hypothesis as

$$C_T^2 = 3.2\chi\epsilon^{-1/3}, \quad \textbf{(7)}$$

where ϵ is the turbulent energy dissipation rate and χ the destruction rate of potential temperature variance σ_θ^2. Bougeault *et al.* [5] and Masciadri *et al.* [6] utilized mesoscale models with a turbulence closure scheme [29] that has a prognostic equation for the turbulent kinetic energy (TKE) e, which allowed the parameterization of ϵ and χ to ultimately obtain C_T^2 according to Eq. (7). He and Basu [30] utilized a different parameterization [31,32] based on e and σ_θ^2 in conjunction with Eq. (7):

$$\epsilon = \frac{(2e)^{3/2}}{B_1 L_M}, \quad \chi = \frac{(2e)^{1/2}}{B_2 L_M}\sigma_\theta^2. \quad \textbf{(8)}$$

Here, L_M is the master length scale combining the characteristic scales of the surface, turbulence, and buoyancy, and the coefficients B_1 and B_2 were found to be equal to 24 and 15, respectively, from numerical simulations. He and Basu used the high-order MYNN 2.5 turbulence closure scheme [33,34] with a prognostic output of e and diagnosed σ_θ^2 and L_M. Physically, the TKE per unit mass is half the sum of the velocity field variances: $e = (\sigma_u^2 + \sigma_v^2 + \sigma_w^2)/2$. This variance-based approach based on He and Basu (HB15-var), combined with the MYNN 2.5 turbulence closure scheme in WRF, is also used in the present work. While the variances e and σ_θ^2 and the length scale L_M are available from the WRF model output, they are not contained in the CESAR data product available for this study. Additionally, L_M as used in MYNN-2.5 requires evaluating a vertical integral of TKE from the surface until the boundary layer height [35], which is difficult to obtain experimentally. Consequently, we apply HB15-var only to the simulated meteorology.

B. Scintillometer Observations of C_n^2 at the CESAR Site

The accuracy of the estimated C_n^2 values is assessed by comparing them against C_n^2 measurements from two scintillometers deployed at the CESAR site. The instruments are mounted at two heights: ∼10 m and ∼80 m. Therefore, the lower instrument is almost always situated in the SL so that it serves as a reference for all three parameterizations. That is not the case for the higher instrument because the SL height regularly falls below the mounting height, for example, during the night (all seasons) and partially during the day (non-summer seasons). Consequently, we only utilize that higher scintillometer as a reference for the variance-based method.

A scintillometer consists of a transmitter and receiver displaced over a horizontal path between 0.1 km and 10 km. The transmitter emits a beam of light at one end of a horizontal path, and the receiver receives it at the other. C_n^2 is then derived from measured fluctuations of received optical power caused by the OT along the path [36]:

$$C_n^2 = 1.12D^{7/3}\Lambda^{-3}\sigma_{\ln(I)}^2, \quad \textbf{(9)}$$

where D is the scintillometer aperture size, Λ is the path length between transmitter and receiver, and $\sigma_{\ln(I)}^2$ is the log-variance statistic of the intensity fluctuations, I. The two scintillometers are part of the Dutch Ruisdael observatory infrastructure and measure along two almost perpendicular paths as indicated by the solid and dashed lines in Fig. 3. In particular, there are

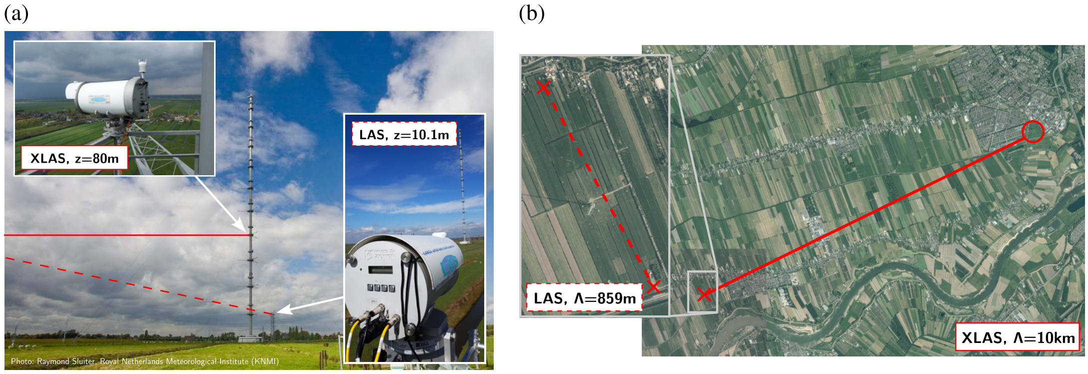

Fig. 3. Vertical placement and approximate measurement paths of the two scintillometers—LAS (dashed line) and XLAS (solid line)—at the CESAR site as seen (a) from the Cabauw field and (b) on an aerial photograph.

1. A Kipp&Zonen MKII Large Aperture Scintillometer (LAS, $D = 0.147$ m), measuring along a $\Lambda = 859$ m path (dashed line) at 10.1 m height above ground, and
2. A Kipp&Zonen MKI eXtra Large Aperture Scintillometer (XLAS, $D = 0.32$ m), which has been upgraded to MKII specifications, measuring along a $\Lambda = 10$ km path (solid line) at $\sim$80 m height.

The panels in Fig. 3 show the approximate (a) vertical and (b) horizontal scintillometer measurement paths. Both scintillometers operate at a wavelength of $\lambda = 850$ nm and have a finite aperture to ensure they are saturation resistant over longer path lengths [36]. In calculating $\sigma^2_{\ln(I)}$ from the raw 1 kHz recorded data series of I, a high pass filter of 30 s was applied to filter out absorption fluctuations, and intervals with less than 20% of available data were set to a dummy value. The intensity data are aggregated into 30 min bins from which C_n^2 is computed. In a quality control step, C_n^2 measurements are classified as unreliable and discarded if the received mean carrier power drops below a setup-dependent threshold. This happens, for example, during heavy rainfall or fog at the CESAR site, resulting in severe attenuation or loss of the scintillometer signal.

C. Meteorological Observations within the Surface Layer

Several meteorological variables serve as input for the different parameterizations to estimate C_n^2 at the 10 m level (surface layer) and compare it to the corresponding scintillometer observations. These measurements are extracted as 10 min averages from the instruments mounted on and around the 200 m high Cabauw tower of the CESAR site [cf. Fig. 3(a)]. In particular, we utilize the profiles of air temperature $\overline{T}(z)$ and horizontal wind measured at 2 m (T only), 10 m, and 20 m, above ground, respectively, to estimate $\Gamma(z)$ and $S(z)$ at the 10 m level. The horizontal wind at CESAR is measured with cup anemometers and wind vanes [17] from which we obtain the horizontal components $\bar{u}(z)$ and $\bar{v}(z)$ for the computation of $S(z)$. Details about the gradient computation are presented in Supplement 1. From those gradients, C_T^2 at 10 m height is estimated following W71/HB16-grad. The turbulent fluxes u_* and $\overline{w'\theta'}$ for the corresponding W71-flux C_T^2 estimates are obtained from an eddy covariance system consisting of an open-path H_2O/CO_2 sensor (LICOR-7500) and a sonic anemometer (Gill-R50) mounted at 3 m height [17]. Following the surface layer assumption, the fluxes are considered to be height invariant and also valid at 10 m height. As mentioned before, the variances required for HB15-var are not routinely available from CESAR, and the experimental determination of the length scale L_M is challenging. Consequently, only the gradient- and the flux-based methods are utilized in conjunction with the observed meteorology.

Converting C_T^2 to C_n^2 following Eq. (1) is the same for all three parameterizations and requires the Bowen ratio β and the 10 m atmospheric pressure. The latter, P_{10}, is computed from the reference sea-level pressure P_0, utilizing the hypsometric equation and the 10 m temperature. The β-based C_n^2 humidity correction is based on the dynamic sensible heat flux Q_H and the latent heat flux Q_L. Q_H (in W/ m^{-2}) is converted from the measured kinematic sensible heat flux $\overline{w'\theta'}$ (in m K s^{-1}) to its dynamic form as $Q_H = \rho c_p \overline{w'\theta'}$ with the density ρ and the specific heat capacity c_p of air [24]. The corresponding latent heat Q_L is also measured by the eddy covariance system at 3 m above ground [17]. We refer to all these observed meteorological variables for C_n^2 estimation as MET data for the rest of the study.

D. Mesoscale Simulation Setup

The same variables observed at the CESAR site are numerically obtained by running one WRF simulation per test case. All simulations are forced with the ERA5 reanalysis data [37] provided by the European Centre for Medium-Range Weather Forecasts (ECMWF). The horizontal grid size of ERA5 is $\sim$30 km, and three nested WRF domains are used to bring the horizontal grid size down to 1 km in the finest domain (cf. Table 1). WRF produces instantaneous snapshots of all variables every 10 min, matching the temporal sampling rate of the CESAR observations. Panels (a) and (b) of Fig. 4 depict how the CESAR site is represented as a gridded WRF domain. A vertical cross-section (cf. panel (a)) is extracted using bilinear interpolation along the path shown in panel (b). This plane (approximately) contains the Cabauw tower at the very left and the path of the XLAS (red solid line) in the horizontal direction. The average heights of the model pressure levels plotted as gray lines show that the WRF model has a vertical resolution close to the surface of $\sim$25 m with the first level at $\sim$9 m. The bell-shaped function plotted

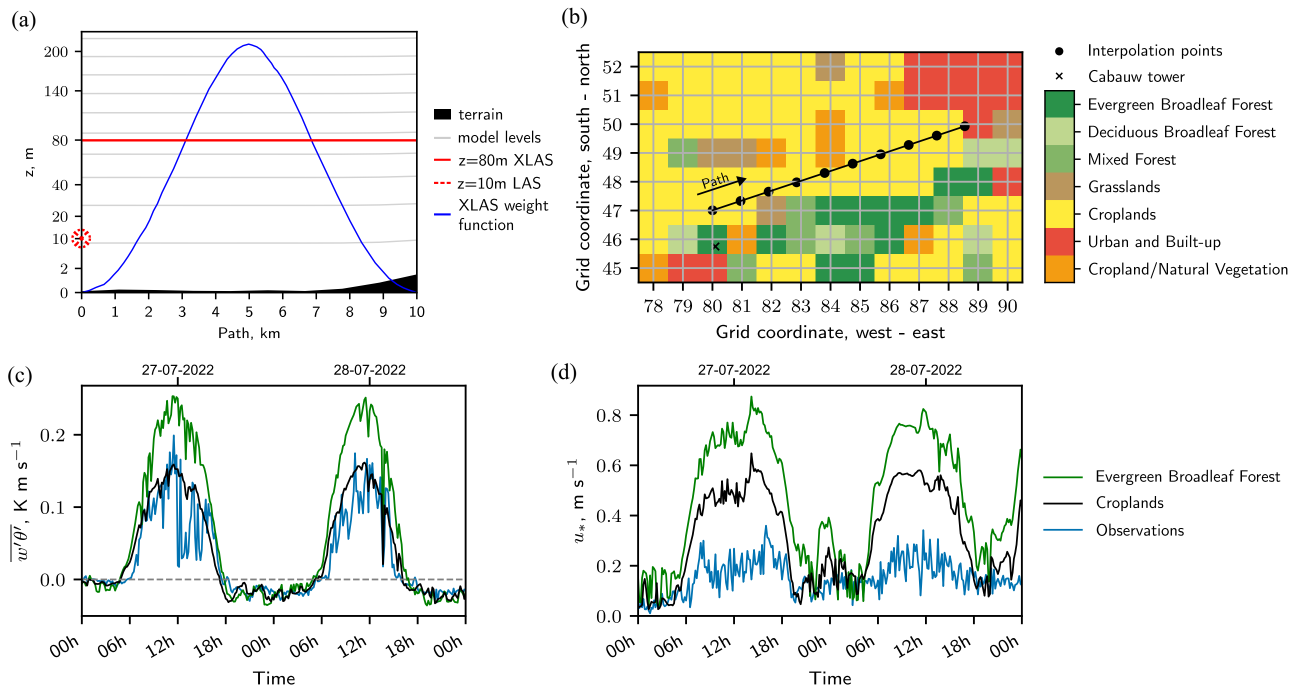

Fig. 4. Representation of the CESAR site in WRF. (a) Domain cross-section containing 10 km XLAS path with model levels in gray and LAS/XLAS weighing function in blue; (b) MODIS land use classes of CESAR site (cross) and its surroundings; effect of different land use classes on (c) sensible heat flux and (d) friction velocity.

Table 1. Nested Domain Configuration Used for All Test Cases in WRF

Domain	Horizontal Resolution	# Grid Points	# Vertical Levels
D01	9 km × 9 km	128 × 100	101
D02	3 km × 3 km	124 × 127	101
D03	1 km × 1 km	130 × 127	101

as solid blue line is the LAS/XLAS weighing function related to the scintillometers' path-averaging effect. The function's peak at half the path length means that turbulence in the path's center contributes strongest to the measured C_n^2 [3].

The aerial pictures in Fig. 3(b) show that land use around the CESAR site is diverse. This heterogeneity of the surroundings—crop fields, grassland, urban areas—is represented in WRF through the 21-category IGBP-MODIS land-use dataset [38,39]. Based on that dataset, one land-use class is automatically assigned to each surface grid point during WRF preprocessing, as shown in Fig. 4(b). Here, only the seven classes relevant to the selected area are shown. Depending on the assigned land-use class, the WRF model uses different values for, e.g., surface roughness (cities cause more drag than grassland) or heat capacity (water bodies have larger heat capacity than croplands), while solving for the various simulated variables. These surface-specific parameters are, for example, used by the surface layer scheme that solves for the surface fluxes based on Monin Obukhov similarity theory [40,41]. The fluxes are then used in the flux-based C_n^2 parameterization, so an incorrectly assigned land-use class can cause systematic deviations between simulated values at one grid point and collocated observations. Such a land-use misclassification happens at grid point (80, 46), closest to the Cabauw tower. This grid point is classified as "evergreen broadleaf forest" although the aerial photos in Fig. 3 indicate croplands or grasslands for the CESAR site. Only the neighboring grid point (80, 47) is classified as "croplands," which seems more realistic. The effect of this misclassification on sensible heat flux $\overline{w'\theta}$ and friction velocity u_* is visible in panels (c) and (d) of Fig. 4. The forest-type land-use class (green curve) leads to significantly larger values for both variables than the "croplands" class (black curve). More importantly, the lower values of the "croplands" time series agree better with observations from Cabauw (blue curve). The notably lower observed u_* in Fig. 4(d) is likely due to the local smoothness of the CESAR site [26], which WRF misses due to its coarse resolution. Still, u_* associated with the "croplands" class is assumed more realistic than the "forest" one. Since the W71-flux approach takes $\overline{w'\theta'}$ and u_* as inputs, these variables must be simulated realistically by WRF. We, therefore, select grid point (80, 47) as representative of the CESAR site and as the starting point of the extracted cross-section.

The selected physics schemes utilized by WRF to represent various processes in the atmosphere are listed in Table 2, and the corresponding WRF configuration files (`namelist.input` files) are provided on Github [46]. Most relevant for this study is the selection of the planetary boundary layer (PBL) scheme. The PBL scheme parameterizes the sub-grid turbulence, i.e., the turbulent processes within the boundary layer (first few kilometers of the atmosphere) and clean air turbulence in the free atmosphere (above the PBL). Such parameterizations are required because the grid size of mesoscale models is too coarse to explicitly resolve turbulence (to explicitly resolve turbulence, one can run large-eddy simulations with $\mathcal{O}(10\ \mathrm{m})$ resolution can be run

Table 2. Physics Schemes Used in WRF for All Test Cases to Parameterize Atmospheric Processes

Physical Process	Scheme
Surface layer	Mellor–Yamada–Nakanishi–Niino (MYNN) [40]
Boundary layer	MYNN 2.5 [33,34] with eddy-diffusivity/mass-flux [35] (EDMF)
Microphysics	WSM-5 [42]
Radiation (long and short-wave)	Rapid radiative transfer model for GCMs (RRTMG) [43]
Land surface model	Noah LSM [44] with IGMP-MODIS 21-category land use data [38,39]
Cumulus parameterization	Modified Kain–Fritsch scheme [45] (D01 only)

to explicitly resolve turbulence. The WRF model outputs different variables depending on the selected PBL scheme, so the PBL scheme selection can constrain the C_n^2 parameterizations that can be applied. We utilize the higher-order Mellor–Yamada–Nakanishi–Niino (MYNN) turbulence scheme in its 2.5-order closure version with eddy-diffusivity/mass-flux [35] (EDMF) option enabled. MYNN-2.5 is a high-order PBL scheme that solves for TKE e and variance of potential temperature σ_θ^2, which are required for variance-based C_n^2 parameterizations. Not all PBL schemes available in WRF provide TKE, and only MYNN 2.5 and MYNN 3 yield σ_θ. Since we found MYNN 3 to be numerically unstable in some cases, MYNN 2.5 is the only PBL scheme suitable for this comparison. Outside this study, if only gradient- or flux-based techniques are of interest, all other WRF PBL schemes are applicable. To determine the domain of applicability for the MOST-based C_n^2 parameterizations, we utilize the PBL height from the MYNN scheme and compute the SL height as 10% of that variable. The same estimated SL height is utilized for WRF- and MET-based C_n^2 estimates to ensure comparability between the parameterizations.

Post-processing the WRF model outputs with the C_n^2 parameterizations yields estimates of C_n^2 at each model grid point with 1 km horizontal spacing. Scintillometers, however, yield integrated C_n^2 values caused by the turbulence along the measurement path. In cases where this path crosses multiple WRF grid cells, the simulated C_n^2 estimates need to be aggregated to align them with the observations. This consideration is essential for the 10 km XLAS. As mentioned, we horizontally interpolate the WRF grid to extract a vertical cross-section containing the scintillometer path. Next, we vertically interpolate the cross-section levels to the path height (here 80 m AGL). Finally, a path-averaged C_n^2 estimate is computed using the scintillometer path weighting function [36] [see also Fig. 4(a)]. The bell-shaped weighing function of an LAS/XLAS puts the most weight on the center of the path. In the case of the LAS, where the path length of 859 m is comparable to the grid resolution, we compare the observations against values from the grid point closest to the link's center, i.e., the starting point of the extracted cross section.

E. Performance Metrics

The agreement between any pair of observed $\log_{10} C_n^2$ time series of length n, $\{o_1, \ldots, o_i, \ldots o_n\}$, and its estimated counterpart, $\{f_1, \ldots, f_i, \ldots f_n\}$, is quantified in $\log_{10}$-space through three metrics: the constant bias between the two time series, the centered root-mean-squared error (cRMSE), and Pearson's correlation coefficient r. The bias is computed as the difference between the mean values of both signals, $\bar{f}$ and $\bar{o}$, as

$$\mathrm{Bias} = \bar{f} - \bar{o}, \tag{10}$$

and it quantifies the constant shift between the two. The cRMSE is defined as

$$\mathrm{cRMSE} = \frac{1}{n}\sum_{i=1}^{n}\left[(f_i - \bar{f}) - (o_i - \bar{o})\right]^2, \tag{11}$$

and it quantifies the average error throughout the signal after removing the bias. Additionally, the Pearson correlation coefficient r, defined as

$$r = \frac{\sum_{i=1}^{n}\left(f_i - \bar{f}\right)(o_i - \bar{o})}{n\sigma_f\sigma_o}, \tag{12}$$

reflects how well the estimate matches the observation's pattern (e.g., diurnal cycle). Here, σ_f and σ_o are the standard deviations of the simulated and observed time series, respectively. For all metrics, the estimated C_n^2 time series are clipped to a minimum value of $C_n^2 \approx 10^{-16}\ \mathrm{m}^{-2/3}$ before computing the scores. That is done to avoid an unreasonably large contribution of estimation errors in the weak turbulence regime, which are exaggerated by the $\log_{10}$ scaling. The $10^{-16}\ \mathrm{m}^{-2/3}$ threshold is commonly used in FSOC and optical astronomy literature to separate out weak and almost negligible OT strength [47–50]. To match the different temporal sampling rates of the scintillometer observations (30 min) and the WRF/MET estimates (10 min) for the score computation, we downsample the 10 min data. More specifically, each 30 min scintillometer sample is matched by selecting the 10 min sample of the WRF/MET data that falls into the middle of the 30 min interval. We prefer this approach over, e.g., averaging three 10 min samples into one 30 min sample because we would like to retain the larger variability typically exhibited by flux measurements compared to, e.g., mean wind measurements.

3. RESULTS

In the following, the performance of each C_n^2 parameterization, with WRF and MET inputs, is compared against the scintillometer observations at 10 m and 80 m height (cf. Table 3 for a result overview). We begin in Section 3.A with a surface layer-bound comparison. The MOST-based parameterizations—W71-flux and W71/HB16-grad—are compared to observations from the 10 m high LAS. The 80 m high XLAS is not considered for this part of the analysis because the number of valid C_n^2 estimates is low due to the SL assumption. In other words, for long periods of time (especially in spring and autumn), the SL is too shallow to contain the high scintillometer, rendering the flux and gradient-based methods inapplicable. Consequently, the

Table 3. Overview of Evaluated Combinations of Input Data—Observed (MET) or Simulated (WRF) Meteorology—and C_n^2 Parameterizations for the Two Scintillometers Mounted at Height z and Measuring along Path of Length Λ

	MET Input			WRF Input		
Scintillometer	**W71-flux**	**W71/HB16-grad**	**HB15-var**	**W71-flux**	**W71/HB16-grad**	**HB15-var**
$z = 10$ m, $\Lambda = 859$ m	yes	yes	no obs. data	yes	yes	yes
$z = 80$ m, $\Lambda = 10$ km	no, beyond SL	no, beyond SL	no obs. data	no, beyond SL	no, beyond SL	yes

statistical significance of such a comparison is low, and it would not be insightful. In contrast, the variance-based C_n^2 estimates are valid everywhere in the boundary layer, so we go beyond the SL in Section 3.B and assess the accuracy of the variance-based C_n^2 at both scintillometer levels. Here, only WRF data are used as inputs to HB15-var due to the unavailability of turbulent variances within the CESAR data product.

A. Three-way Comparison of C_n^2 Parameterizations in the Surface Layer

Figure 5(a) presents the estimated and the observed 10 m level C_n^2 time series for all three test cases. The figure serves as a three-way comparison between observed SL C_n^2 and the effect of different input data (WRF or MET) when using the same C_n^2 parameterization or the impact of using the same data but different C_n^2 approaches (flux- or gradient-based). The shading of the background indicates static atmospheric stability based on the simulated sensible heat flux: stable conditions ($\overline{w'\theta'} < 0$), typically present during the night, are shaded in gray, and unstable conditions ($\overline{w'\theta'} > 0$), generally present during the day, are shaded in white. Most estimated curves show substantial dips to low C_n^2 values at the time of transition between stability (i.e., during neutral conditions). That is where the time series clipping to a minimum of $C_n^2 = 10^{-16}\ \mathrm{m}^{-2/3}$ (dotted lines) takes effect to avoid the unfair contribution of these negligibly low turbulence conditions. The gaps in the estimated time series stem from the SL being too shallow even for the 10 m LAS, while gaps in the observed scintillometer time series are due to low received power likely related to fog.

Bias, cRMSE, and correlation r for each pair of observed and estimated C_n^2 time series are displayed in Fig. 6. The table follows the same structure as the time series plots, with flux-based results in columns (a) and (b) and the gradient-based results in columns (c) and (d). For ease of comparison, columns (e) and (f) contain the variance-based results for C_n^2 estimation beyond the surface layer, which are discussed in the following section. The rows break the scores down by test case and stability, and the cell colors allow for visual interpretation of the score values with respect to the color bars.

Overarching comparison of the W71-flux and W71/HB16-grad in Fig. 5(a) reveals that both approaches, regardless of input data, generally match the pattern of the observations. For example, low-turbulence dips during neutral conditions or strong turbulence peaks during the day are timed mostly well, resulting in mostly high-correlation coefficients in Fig. 6. Only the MET + Flux (stable) comparison hints toward a seasonal performance dependency with lower r and higher cRMSE in spring and autumn compared to summer. The remaining cases show comparable performance throughout all seasons. Comparing the scores of the variance-based estimates (WRF + Var, (e) and (f)) against the flux and gradient-based approaches indicates an overall more balanced error behavior of WRF + Var with less variation of all metrics between day and night, which is discussed in detail in Section 3.B.

Despite the good overall performance, the W71-flux and W71/HB16-grad show significant biases during stable conditions upon detailed inspection. The nighttime bias is especially large for W71/HB16-grad, regardless of season. With WRF inputs, the nighttime 10 m signal is overestimated by about one order of magnitude, whereas the estimates from MET input show a consistent underestimation of almost one order of magnitude. During unstable conditions, both WRF + Grad and MET + Grad slightly overestimate the C_n^2 values. These deviations could be related to too-strong (C_n^2 overestimation) or too-weak (C_n^2 underestimation) gradient estimates due to the coarse spacing of the sensors and model levels. For both input data, the gradients have to be computed numerically from levels separated by multiple meters, which is known to lead to deviations [51]. Also, the similarity relationship between C_T^2 and the gradients might be erroneous. In the case of the flux-based C_n^2, WRF and MET inputs both lead to overestimating the nighttime values. The underlying observed and simulated nighttime fluxes show realistic values and orders of magnitude, which does not allow us to explain this behavior. The deviation seems systematic and could point to a weakness of W71-flux during the night, but a final conclusion would require an extensive analysis beyond the scope of this work.

Another difference between the C_n^2 estimates is the smoothness of the estimated signals. The gradient-based estimates are smoother (i.e., show fewer fluctuations) than the flux-based estimates, also visible in the lower cRMSE values for W71/HB16-grad. Again, the effect is more pronounced at night than during the day for all cases. Strong fluctuations of multiple orders of magnitude are observed during the 2nd night in autumn for the MET + Flux estimate. Here, the observed sensible heat flux is very close to zero, where the W71-flux parameterization is very sensitive, resulting in the depicted large jumps. Smoothness also differs between the two WRF-based estimates and their MET-based counterparts: the WRF-based results are smoother than the MET-based ones, which is expected since WRF's 1 km grid resolution is not fine enough to capture very local or short-lasting phenomena. For example, the large drop of C_n^2 during the first day of the summer case at ca. 12:00Z is entirely missed by WRF + Flux and WRF + Grad but captured well by the MET-based estimates.

Despite the discussed errors, both approaches yield consistently good estimates of daytime C_n^2, regardless of the utilized input data. Additionally, the generally good agreement between

(a) Three-way comparision of flux and gradient-based C_n^2 estimates at the 10 m level only within the surface layer.

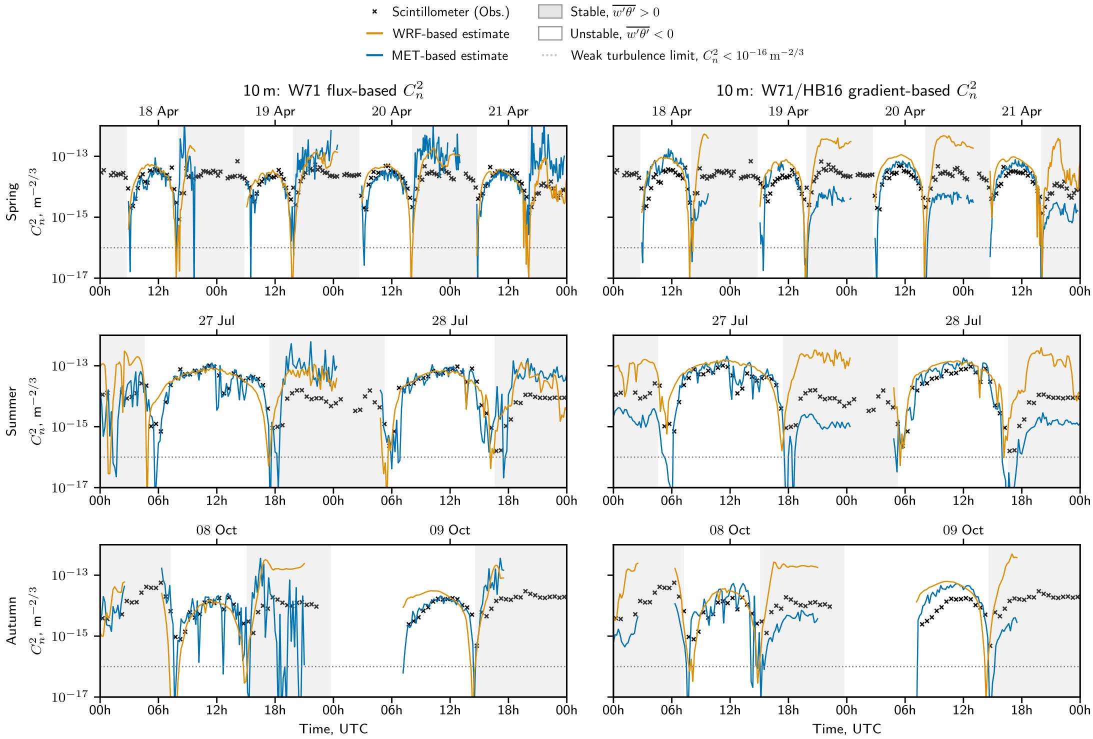

(b) Multi-level comparison of variance-based C_n^2 estimates within the surface layer (10 m height, LAS) and beyond (80 m height, XLAS). No variance-based estimates with MET inputs are made because of limited data availability.

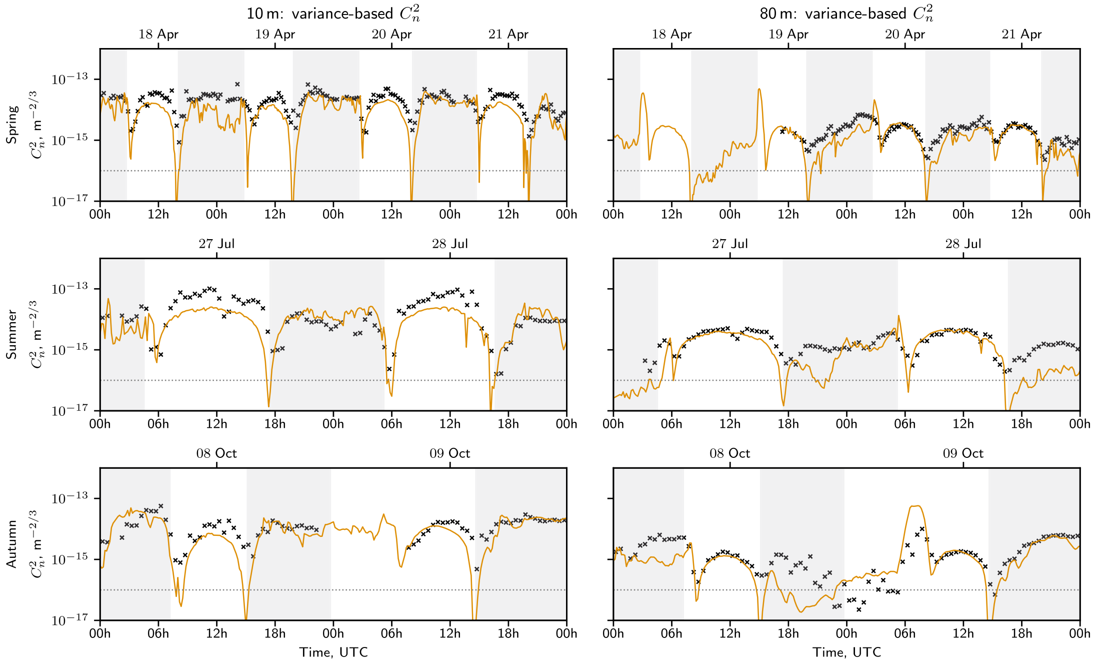

Fig. 5. Comparison of observed C_n^2 from scintillometers (black markers) against C_n^2 values estimated with three different parameterizations from simulated (orange) or observed (blue) meteorology. The rows in panels (a) and (b) correspond to the three test cases: spring (April 18–22, 2022), summer (July 27–29, 2022), and autumn (October 8–10, 2022).

WRF-based and MET-based C_n^2 estimates (leaving the biases aside) is promising because it indicates that our WRF configuration reproduced the observed meteorology reasonably well.

B. Beyond the Surface Layer: Performance of the Variance-based C_n^2 Parameterization

So far, the discussion has focused on the SL, applying gradient and flux-based methods to 10 m observed or simulated

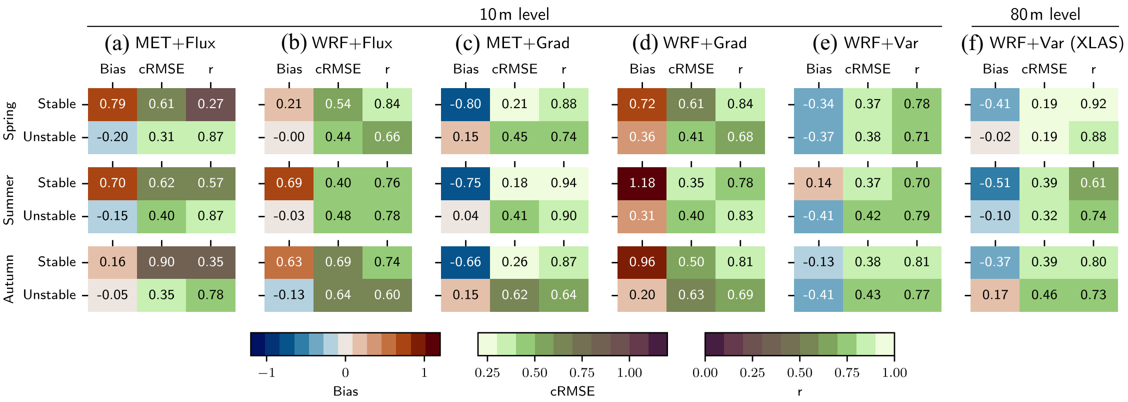

Fig. 6. Bias, centered RMSE, and correlation coefficient r, quantifying the agreement between the observed and estimated $\log_{10} C_n^2$ time series (cf. Fig. 5). Columns (a)–(f) present the performance of the different combinations of input data (MET or WRF) and C_n^2 parameterizations with respect to scintillometer observations. The low values of all estimated time series are clipped to $C_n^2 = 10^{-16}\ \mathrm{m}^{-2/3}$ before computing the scores to avoid unfair dominance of negligibly weak turbulence in $\log_{10}$-space.

meteorological variables. We now employ the variance-based method to estimate C_n^2 at higher altitudes and compare the results to scintillometer measurements from two heights: 10 m and 80 m above ground. Due to the difficulty to experimentally determine L_M and because of the limited availability of TKE and σ_θ^2 in the CESAR data product, we only utilize data from the WRF model for this comparison. The estimated C_n^2 time series derived from WRF (WRF + Var) for both altitudes are shown in Fig. 5(b). The 10 mC_n^2 values (within the SL) are depicted in the left column and the 80 mC_n^2 curves (often beyond the SL) in the right column. The previously discussed Fig. 6 also includes the performance scores that assess agreement between the WRF + Var estimates and the observed data for easy comparison with the other approaches.

Similar to the SL results, the overall agreement of WRF + Var with observations is good. During most nights, C_n^2 matches the scintillometer data at both heights well in terms of magnitude and correlation. The daytime C_n^2 estimates also reflect the trends well by means of correlation, but WRF + Var consistently underestimates the daytime magnitude at the 10 m level. This behavior cannot be observed at the 80 m level where daytime C_n^2 is captured with high accuracy as quantified by the low biases. Interestingly, the trend reverses for stable conditions with larger biases at the 80 m level and lower biases at the 10 m level. The reason could be that WRF misses SL contributions to the turbulence during the day and some higher altitude effects during the night. Such systematic discrepancies are common in numerical weather modeling because the complex physical processes of our atmosphere have to be simplified or approximated, e.g., to keep the models' computational complexity reasonable [52].

Along those lines, we attribute the three notable trend deviations at night between WRF + Var and the scintillometers [cf. Fig. 5(b)] to complex and/or local weather phenomenona. Such weather patterns are difficult to capture in WRF due to its coarse resolution. One deviation occurs in spring at the 10 m level (18/19 April, 0:00Z–6:00Z) and two others at the 80 m level in summer (27/28 July, 18:00Z–00:00Z) and autumn (8/9 October, 18:00Z–6:00Z). The signal degradation experienced by both scintillometers during the autumn deviation supports the assumption that a complex weather pattern is present. The observed 80 mC_n^2 drops to very low values and exhibits increased scattering, while the corresponding 10 mC_n^2 observations fail quality control and are discarded. It seems that WRF captured the weather event leading to the signal degradation but with a different timing.

Despite the discussed periods of temporarily low performance, the results are overall satisfying. There is no clear seasonal trend of the performance (visually and quantitatively), and the correlation between estimated and observed C_n^2 is high for both heights as reflected by the scores in Figs. 6(e) and 6(f). When directly compared to the flux and gradient-based alternatives, the variance-based C_n^2 correlation values are lower in some cases at 10 m height but show less variation between stability conditions. We note that the scores of the MOST-based approaches are based on fewer samples for atmospheric stable conditions due to the SL constraint, so the statistical uncertainty is expected to be higher. The biases of the variance-based C_n^2 estimates are mostly negative, indicating a consistent underestimation of turbulence strength up to half an order of magnitude. This underestimation trend of WRF + Var contrasts the more variable performance of W71-flux and W71/HB16-grad, which show lower (absolute) biases during the day but significantly higher (absolute) biases during the night. In general, the error behavior of WRF + Var seems more balanced with similar r and cRMSE values throughout seasons and atmospheric stability conditions compared to the other methods. This observation is confirmed visually by comparing the WRF + Var time series [Fig. 5(b)] with those of WRF + Grad and WRF + Flux [Fig. 5(a)]: the WRF + Var curves track the scintillometer observations more consistently for all test cases, day and night, and for both heights. Consequently, HB15-var seems to be the more reliable choice for C_n^2 estimation from WRF than the other two methods, and it has the additional advantage of being applicable anywhere in the boundary layer.

4. CONCLUSION

We applied three distinct C_n^2 parameterizations to observed and simulated meteorological variables and compared the resulting C_n^2 estimates to measured C_n^2 evolutions from two scintillometers mounted at different heights and measuring at paths of different lengths. The parameterizations utilized either (a) vertical gradients of the mean wind and temperature fields, (b) turbulent fluxes, or (c) turbulent variances to estimate C_n^2. The meteorological inputs were either experimentally obtained (MET) at the Cabauw Experimental Site for Atmospheric Research (CESAR) in the Netherlands or produced as mesoscale hindcast of the same site by the Weather Research and Forecasting (WRF) model. The variance-based method was only applied to WRF model data because observed MET variances are not routinely available and because the experimental estimation of the associated length scale is challenging. Three multi-day test cases from spring (4 days), summer (2 days), and autumn (2 days) were selected to investigate the seasonal variability of the parameterizations' performance. While our study is focused on CESAR due to its extensive instrumentation, we anticipate our results to be valid also for comparable sites.

Overall, all three parameterizations performed well during stable (nighttime) and unstable (daytime) conditions and did not show a significant seasonal accuracy dependency. Detailed analysis revealed that the flux and gradient-based methods yield large constant biases up to one order of magnitude for stable/nighttime estimates compared to measured C_n^2. In contrast, the unstable/daytime values are close to observations. Because both parameterizations are more sensitive to their inputs during stable than unstable conditions, this finding stresses the need to accurately model or measure the parameterization inputs, especially at night. The variance-based approach tends to underestimate the night and day values but shows high correlation. Since we do not have access to the measured turbulent variances, we cannot investigate whether the underestimation results from the variance-based formulation or the simulated data. Nevertheless, the overall error behavior was more balanced compared to the other two methods, with less variation in the performance metrics for different seasons and atmospheric stabilities. Concerning the input data, the WRF-based estimates were found to be as realistic as the MET-based ones compared to the scintillometers. The cases where WRF deviates from observed trends can typically be attributed to local or complex short-duration weather events. Such patterns are known to be challenging to model in mesoscale simulations. Due to the statistically high accuracy of the WRF-based results, we still consider them reliable and valuable for quantifying important trends.

For FSOC purposes, the selection of a C_n^2 parameterization is highly use case dependent. The typical goal is to quantify optical turbulence (OT) strength at or around a site of interest by determining C_n^2 experimentally or numerically to feed it to FSOC downstream tasks. Such tasks can be the design of adaptive optics systems at a laser terminal [18] or the quantification of the effect that OT has on a propagating beam [53]. The details of the respective use cases guide the selection of an appropriate parameterization. It matters, for example, whether a simulation or a field campaign is carried out and how the FSOC link under consideration is set up (e.g., vertical or horizontal). In the case of field campaigns, the flux and gradient-based methods are most relevant due to the challenging length scale estimation required for the variance-based parameterization. The gradient-based approach only requires simple routinely available mean values of meteorological variables but from multiple instruments at different heights. The flux-based method, however, utilizes turbulent fluxes from more expensive instruments but only needs observations close to the surface. Consequently, the instruments available for a field campaign can constrain the choice of parameterization. In WRF, fluxes and the underlying fields for the gradients are routinely available. However, the numerical computation of gradients can introduce additional errors [51], and the fluxes strongly depend on the selected land use dataset, which needs to be representative of the site being simulated. Also, the theoretical foundation of both parameterizations—Monin Obukhov similarity theory (MOST)—only allows their application inside the constant-flux surface layer (SL), which varies in depth throughout the day. Therefore, for example, MOST-based C_n^2 estimates for FSOC terminals or terrestrial links are only valid when they are fully contained in the SL.

The SL restriction does not apply to the variance-based method. This approach can be utilized for the entire atmosphere but requires outputs from a mesoscale model (e.g., WRF) configured with a high-order turbulence closure scheme. We envision that such variance-based C_n^2 estimates based on WRF (WRF + Var) can be utilized to assess the behavior of various FSOC links. For example, the long 10 km path of the 80 m high scintillometer used in this study could be viewed as an intra-city link with terminals mounted on high-rise buildings. Similarly, the lower scintillometer with 859 m path length indicates the applicability of WRF + Var also for shorter links where the length is similar to the horizontal resolution of the mesoscale model. Resolving even shorter links of $\mathcal{O}(100\text{m})$ requires to run gray-zone or large eddy simulations [54]. WRF supports both, and we do not see a fundamental limitation of the variance-based parameterization, which should hinder its successful application. Nevertheless, the accuracy of the C_n^2 estimates in these cases must be assessed in future work. We also see the potential to analyze OT along links between space and ground using WRF + Var. While our study did not focus on such high-altitude applications, Basu *et al.* [12] demonstrated good agreement between variance-based C_n^2 and observed C_n^2 from thermosondes up to ~25 km height. Combined with the balanced error behavior and the overall good performance demonstrated in our work, we believe that the mesoscale simulations and variance-based C_n^2 estimates can be very useful for the optics community.

In conclusion, our study presents the differences between three main classes of C_n^2 parameterizations concerning stability-dependent performance, theoretical limitations, and relevance for FSOC applications. The selection is highly use case dependent, but it generally seems that the gradient and flux-based approaches are better suited for near-surface field campaigns, while the variance-based method, in combination with a mesoscale model, has advantages for numerical studies across the entire atmosphere.

Funding. Nederlandse Organisatie voor Wetenschappelijk Onderzoek (P19-13, 184.034.015).

Acknowledgment. This publication is part of the project FREE—Optical Wireless Superhighways: Free photons (at home and in space) of the research programme TTW-Perspectief, which is (partly) financed by the Dutch Research Council (NWO). We are grateful for the observational data provided by Royal Netherlands Meteorological Institute (KNMI) and the Ruisdael

Observatory, a scientific research infrastructure, which is (partly) financed by the Dutch Research Council (NWO).

Disclosures. The authors declare no conflicts of interest.

Data availability. The post-processed WRF simulation and MET data are available from [55]. The `namelist.input` files to run the simulations and the scripts to obtain the presented results are available on Github [46]. The meteorological observations of the CESAR site are publically available through the data platform of the Royal Netherlands Meteorological Institute [56]. The scintillometer validation data are not publicly available at this time but may be obtained from the authors upon reasonable request.

Supplemental document. See Supplement 1 for supporting content.

REFERENCES

1. A. Jahid, M. H. Alsharif, and T. J. Hall, "A contemporary survey on free space optical communication: Potentials, technical challenges, recent advances and research direction," J. Netw. Comput. Appl. **200**, 103311 (2022).
2. H. Kaushal and G. Kaddoum, "Optical communication in space: challenges and mitigation techniques," Commun. Surveys Tuts. **19**, 57–96 (2017).
3. F. Beyrich, O. K. Hartogensis, H. A. de Bruin, *et al.*, "Scintillometers," in *Springer Handbook of Atmospheric Measurements*, T. Foken, ed. (Springer, Cham, 2021), pp. 969–997.
4. J. C. Wyngaard, Y. Izumi, and S. A. Collins, "Behavior of the refractive-index-structure parameter near the ground," J. Opt. Soc. Am. **61**, 1646–1650 (1971).
5. P. Bougeault, C. D. Hui, B. Fleury, *et al.*, "Investigation of seeing by means of an atmospheric mesoscale numerical simulation," Appl. Opt. **34**, 3481–3488 (1995).
6. E. Masciadri, J. Vernin, and P. Bougeault, "3D mapping of optical turbulence using an atmospheric numerical model-I. A useful tool for the ground-based astronomy," Astron. Astrophys. Suppl. Ser. **137**, 185–202 (1999).
7. E. L. Andreas, "Estimating C_n^2 over snow and sea ice from meteorological data," J. Opt. Soc. Am. A **5**, 481–495 (1988).
8. D. L. Hutt, "Modeling and measurements of atmospheric optical turbulence over land," Opt. Eng. **38**, 1288–1295 (1999).
9. S. Basu, "A simple approach for estimating the refractive index structure parameter (C_n^2) profile in the atmosphere," Opt. Lett. **40**, 4130–4133 (2015).
10. R. Frehlich, R. Sharman, F. Vandenberghe, *et al.*, "Estimates of C_n^2 from numerical weather prediction model output and comparison with thermosonde data," J. Appl. Meteorol. Climatol. **49**, 1742–1755 (2010).
11. S. Cheinet, A. Beljaars, K. Weiss-Wrana, *et al.*, "The use of weather forecasts to characterise near-surface optical turbulence," Bound.-Lay. Meteorol. **138**, 453–473 (2011).
12. S. Basu, J. Osborn, P. He, *et al.*, "Mesoscale modelling of optical turbulence in the atmosphere: the need for ultrahigh vertical grid resolution," Mon. Not. R. Astron. Soc. **497**, 2302–2308 (2020).
13. C. Ullwer, D. Sprung, E. Sucher, *et al.*, "Global simulations of C_n^2 using the weather research and forecast model WRF and comparison to experimental results," Proc. SPIE **11133**, 111330I (2019).
14. A. Rafalimanana, C. Giordano, A. Ziad, *et al.*, "Optimal prediction of atmospheric turbulence by means of the weather research and forecasting model," Publ. Astron. Soc. Pac. **134**, 055002 (2022).
15. M. J. Savage, "Estimation of evaporation using a dual-beam surface layer scintillometer and component energy balance measurements," Agric. For. Meteorol. **149**, 501–517 (2009).
16. L. M. J. Kooijmans and O. K. Hartogensis, "Surface-layer similarity functions for dissipation rate and structure parameters of temperature and humidity based on eleven field experiments," Bound.-Lay. Meteorol. **160**, 501–527 (2016).
17. F. C. Bosveld, P. Baas, A. C. M. Beljaars, *et al.*, "Fifty years of atmospheric boundary-layer research at Cabauw serving weather, air quality and climate," Bound.-Lay. Meteorol. **177**, 583–612 (2020).
18. K. A. Broekens, N. J. Doelman, W. A. Klop, *et al.*, "Field test demonstration of adaptive Optics pre-correction for a terabit optical communication feeder link," *International Conference on Space Optical Systems* (Accepted), Vancouver, British Columbia, Canada, 2023.
19. W. C. Skamarock, J. B. Klemp, J. Dudhia, *et al.*, "A description of the advanced research WRF model version 4.3," Technical report UCAR/NCAR (2021).
20. J. H. Gladstone and T. P. Dale, "XIV. Researches on the refraction, dispersion, and sensitiveness of liquids," Philos. Trans. R. Soc. London **153**, 317–343 (1863).
21. L. C. Andrews and R. L. Phillips, *Laser Beam Propagation Through Random Media*, 2nd ed. (2005).
22. M. L. Wesely, "The combined effect of temperature and humidity fluctuations on refractive index," J. Appl. Meteorol. Climatol. **15**, 43–49 (1976).
23. A. F. Moene, "Effects of water vapour on the structure parameter of the refractive index for near-infrared radiation," Bound.-Lay. Meteorol. **107**, 635–653 (2003).
24. R. B. Stull, *An Introduction to Boundary Layer Meteorology* (Kluwer, 1988).
25. P. He and S. Basu, "Extending a surface-layer C_n^2 model for strongly stratified conditions utilizing a numerically generated turbulence dataset," Opt. Express **24**, 9574–9582 (2016).
26. J. W. Verkaik and A. A. M. Holtslag, "Wind profiles, momentum fluxes and roughness lengths at Cabauw revisited," Bound.-Lay. Meteorol. **122**, 701–719 (2007).
27. S. Corrsin, "On the spectrum of isotropic temperature fluctuations in an isotropic turbulence," J. Appl. Phys. **22**, 469–473 (1951).
28. A. N. Kolmogorov, "The local structure of turbulence in incompressible viscous fluid for very large Reynolds numbers," C. R. Acad. Sci. URSS **30**, 301–305 (1941).
29. P. Bougeault and P. Lacarrere, "Parameterization of orography-induced turbulence in a mesobeta–scale model," Mon. Weather Rev. **117**, 1872–1890 (1989).
30. P. He and S. Basu, "Mesoscale modeling of optical turbulence (C_n^2) utilizing a novel physically-based parameterization," Proc. SPIE **9614**, 96140K (2015).
31. G. L. Mellor, "Analytic prediction of the properties of stratified planetary surface layers," J. Atmos. Sci. **30**, 1061–1069 (1973).
32. G. L. Mellor and T. Yamada, "Development of a turbulence closure model for geophysical fluid problems," Rev. Geophys. **20**, 851–875 (1982).
33. M. Nakanishi and H. Niino, "An improved Mellor–Yamada level-3 model: its numerical stability and application to a regional prediction of advection fog," Bound.-Lay. Meteorol. **119**, 397–407 (2006).
34. M. Nakanishi and H. Niino, "Development of an improved turbulence closure model for the atmospheric boundary layer," J. Meteorol. Soc. Jpn. **87**, 895–912 (2009).
35. J. B. Olson, J. S. Kenyon, W. A. Angevine, *et al.*, "A description of the MYNN-EDMF scheme and the coupling to other components in WRF–ARW," Technical Report OAR GSD-61 (National Ocean and Atmospheric Administration, 2019).
36. T.-I. Wang, G. R. Ochs, and S. F. Clifford, "A saturation-resistant optical scintillometer to measure C_n^2," J. Opt. Soc. Am. **68**, 334–338 (1978).
37. H. Hersbach, B. Bell, P. Berrisford, *et al.*, "The ERA5 global reanalysis," Q.J.R. Meteorol. Soc. **146**, 1999–2049 (2020).
38. P. D. Broxton, X. Zeng, D. Sulla-Menashe, *et al.*, "A global land cover climatology using MODIS data," J. Appl. Meteorol. Climatol. **53**, 1593–1605 (2014).
39. NCEP, Modified IGBP MODIS 20-category vegetation (land-use) data.
40. A. J. Dyer and B. B. Hicks, "Flux-gradient relationships in the constant flux layer," Q. J. R. Meteorol. Soc. **96**, 715–721 (1970).
41. P. A. Jiménez, J. Dudhia, J. F. González-Rouco, *et al.*, "A revised scheme for the WRF surface layer formulation," Mon. Weather Rev. **140**, 898–918 (2012).
42. S.-Y. Hong, J. Dudhia, and S.-H. Chen, "A revised approach to ice microphysical processes for the bulk parameterization of clouds and precipitation," Mon. Weather Rev. **132**, 103–120 (2004).
43. M. J. Iacono, J. S. Delamere, E. J. Mlawer, *et al.*, "Radiative forcing by long-lived greenhouse gases: calculations with the AER radiative transfer models," J. Geophys. Res. Atmos. **113**, D13103 (2008).

44. F. Chen and J. Dudhia, "Coupling an advanced land surface–hydrology model with the Penn state–NCAR MM5 modeling system. Part I: model implementation and sensitivity," Mon. Weather Rev. **129**, 569–585 (2001).
45. J. S. Kain, "The Kain–Fritsch convective parameterization: an update," J. Appl. Meteorol. Climatol. **43**, 170–181 (2004).
46. M. Pierzyna, "wrf_cn2_intercomp," GitHub, 2024, https://github.com/mpierzyna/wrf_cn2_intercomp.
47. A. D. Tunick, "The refractive index structure parameter/atmospheric optical turbulence model: $C_n{}^2$," Technical report ARL-TR-1615 (Defense Technical Information Center, 1998).
48. K. Weiss-Wrana and L. S. Balfour, "Statistical analysis of measurements of atmospheric turbulence in different climates," *International Symposium on Remote Sensing*, A. Kohnle, eds., Toulouse, France, 2002, p. 93.
49. E. Masciadri, J. Stoesz, S. Hagelin, *et al.*, "Optical turbulence vertical distribution with standard and high resolution at Mt Graham," Mon. Not. R. Astron. Soc. **404**, 144–158 (2010).
50. A. A. B. Raj and S. Padmavathi, "Quality metrics and reliability analysis of laser communication system," Def. Sci. J. **66**, 175–185 (2016).
51. S. P. Arya, "Finite-difference errors in estimation of gradients in the atmospheric surface layer," J. Appl. Meteorol. **30**, 251–253 (1991).
52. J. Dudhia, "A history of mesoscale model development," Asia-Pacific J. Atmos. Sci. **50**, 121–131 (2014).
53. U. G. Yasa, M. Z. Keskin, Z. G. Figen, *et al.*, "Measuring and modeling the influence of atmospheric turbulence on a 2-μm laser beam," Proc. SPIE **12731**, 1273109 (2023).
54. R. Honnert, G. A. Efstathiou, R. J. Beare, *et al.*, "The atmospheric boundary layer and the "Gray Zone" of turbulence: a critical review," J. Geophys. Res. Atmos. **125**, e2019JD030317 (2020).
55. M. Pierzyna, "Dataset: Intercomparison of flux, gradient, and variance-based optical turbulence C_n^2 parameterizations," Zenodo, 2024, https://doi.org/10.5281/zenodo.10966120.
56. Royal Netherlands Meteorological Institute, "KNMI Data Platform," KNMI, accessed 2024, https://dataplatform.knmi.nl/.